

# Effect of travel speed and stress relief on thin Ti-6Al-4V laser wire deposits

N. Chekir<sup>a</sup>, Y. Tian<sup>a</sup>, R. Gauvin<sup>a</sup>, N. Brodusch<sup>a</sup>, J.J. Sixsmith<sup>b</sup>, M. Brochu<sup>a,\*</sup>

<sup>a</sup> Department of Mining and Materials Engineering, McGill University, Montreal, Quebec, Canada H3A 0C5

<sup>b</sup> Liburdi Automation Inc., Dundas, Ontario, Canada L9H 7K4



## ARTICLE INFO

### Keywords:

Additive manufacturing  
Ti-6Al-4V  
Travel speed  
Heat treatment  
Microstructure characterization  
Mechanical properties

## ABSTRACT

The effect of two travel speeds on thin Ti-6Al-4V buildups produced by Laser Wire Deposition (LWD) has been investigated. A travel speed set at 1.4 mm/s promoted recrystallization of columnar prior  $\beta$  grains into horizontal prior  $\beta$  grains. It was associated with lower strength hardly meeting minimum wrought requirements as set by the AMS4911. On the other hand, it was shown that by increasing the travel speed to 7.2 mm/s, sufficiently high cooling rates are occurring creating a fine  $\alpha + \beta$  basket weave structure, while no recrystallization of the prior  $\beta$  grains has been observed. Tensile properties were improved with strength consistently exceeding minimum wrought requirements. An additional stress relief cycle preserved the effect of deposition parameters on material properties. A strong anisotropy in elongation was associated with the slower travel speed where higher values were derived along the Z direction. While the faster travel speed exhibited isotropic properties. Strengthening of the deposits has been observed following a stress relief cycle.

## 1. Introduction

Additive Manufacturing (AM) of titanium alloy Ti-6Al-4V is a promising process for the aerospace industry in order to substantially reduce part cost and waste generation [1–3]. However, and as of today, producing functional parts with properties meeting or exceeding the industry requirements remains extremely challenging mainly due to the variability in the generated properties induced by the different processes [4–9].

The high interest of the aerospace industry in Ti-6Al-4V is in part due to the excellent strength to weight ratio and corrosion resistance properties that the alloy can develop [10–12]. Aluminum and vanadium are the main alloying elements, stabilizing the hcp  $\alpha$  phase and the bcc  $\beta$  phase respectively at room temperature. During the deposition processes and upon cooling from above the melting temperature (about 1660 °C [10]), Ti-6Al-4V starts to solidify into columnar grains of the  $\beta$  phase as a consequence of highly directional heat extraction. Upon subsequent cooling, an allotropic transformation occurs at 1000 °C  $\pm$  20 °C: platelets of the  $\alpha$  phase precipitate starting at the  $\beta$  grain boundaries and develop into a complex arrangement of  $\alpha$  platelets in a  $\beta$  matrix at room temperature [10].  $\beta$  grains will then be referred to as prior  $\beta$  grains. This final typical microstructure is referred to as  $\alpha + \beta$  basket weave. If temperature of the part is above the martensitic start temperature ( $M_s = 575$  °C) and cooling rates exceed the critical rate of 410 °C/s, a fully martensitic type of structure can be developed usually referred to as  $\alpha'$  [13]. Eventually and due to the complex thermal

history of a deposit induced by the cyclic behavior of the addition of new layers, a gradient in the properties of the resulting microstructure may characterize the print as pointed out by Kelly et al. [14] affecting in turn the generated mechanical properties. This becomes extremely important in Direct Energy Deposition (DED) Additive Manufacturing (AM) processes. Many studies have investigated the structure/properties relationship of DED processes by primarily focusing on room temperature static tensile properties and hardness values. From these studies, three different processes are mainly encountered: Laser Wire Deposition (LWD) [7,15–20], Laser Powder Deposition (LPD) [8,9,14,21–30] and the so-called Shape Metal Deposition (SMD) [7,15,31–35] that uses a Tungsten Inert Gas (TIG) torch as a focused thermal energy source to fuse the deposited material.

Travel speed, material deposition rate and laser power are among the most investigated parameters in DED processes [16,18,23,24,32,36–38]. Brandl et al. [16] have shown for instance that by decreasing the laser power, decreasing the deposition rate, or by increasing the travel speed, columnar prior  $\beta$  grains tended to decrease in size affecting in turn mechanical properties. Deposits are also usually reported to display an anisotropic behavior regarding their static tensile property. Tensile samples extracted orthogonal to the build direction have been found in most cases to exhibit higher strengths but lower ductility than samples extracted along the build direction [7–9,15,22,27,31,33]. It was mainly explained with the additional strengthening induced by the presence of columnar prior  $\beta$  grains boundaries orthogonal to the testing direction and the associated grain

\* Corresponding author.

E-mail address: [mathieu.brochu@mcgill.ca](mailto:mathieu.brochu@mcgill.ca) (M. Brochu).

boundary allotriomorphs  $\alpha_{GB}$  [7–9,15,22,27,31,32]. Selection of parameters inducing larger prior  $\beta$  grains such as slow travel speed or higher laser power would reduce tensile strength and increase ductility for samples extracted orthogonally to the build direction. This was explained by the reduced number of macro boundaries through the presence of the larger prior  $\beta$  grains inducing a less important strengthening mechanism [7,8,32]. Regarding LWD microhardness measurements, Brandl et al. [16] have shown that the hardness of the deposited material was always higher than the one of the feedstock. This was reported to be the consequence of an increased solid solution strengthening induced by the enrichment of the melt pool with oxygen and nitrogen. Deposition parameters have also been shown to affect material's microhardness. An increase in travel speed or reduced material feed speed would eventually increase the measured microhardness [16,19].

Stress relieving or aging thermal cycles have been attempted to remove residual stresses while maintaining the developed microstructure [39]. This thermal cycle has been found to not substantially affect the developed microstructure post deposition [7,17,18]. A strengthening of the material has often been reported though [17,18]. One of the common recurrent hypotheses is provided by means of precipitation strengthening of  $Ti_3Al$  [15,18]. But this hypothesis lacks experimental evidence such as TEM observations. This would also require important gradients in chemical distribution of aluminum in order to reach Al concentrations that enable the precipitation of the  $Ti_3Al$  intermetallics [12]. Such gradients were not reported in the literature [18,39]. Another more plausible hypothesis is through solid solution strengthening by diffusion of Al, V, Ti, O and N. This is supported by the study of Brandl and al. [18]. The reported effect of stress relief cycles on static tensile properties is not clear. While some studies imply an increase in strength and a decrease in elongation [15,17], other investigations suggest no real impact of such a thermal cycle on tensile properties [7]. Anisotropy in properties is still reported as in the as-built condition [7,15,17,19,29].

This paper takes advantage of the fully dense microstructure developed by LWD. A simple thermal model is presented to provide a basic understanding on the thermal history experienced by the deposits for the two travel speeds investigated in this study. Structural development mechanisms are then discussed for the two conditions. The beneficial effect of an increase in travel speed on the generated microstructure and the anisotropy in materials properties will then be discussed. A typical stress relief is performed in an attempt to keep the effect of deposition parameters on the developed microstructure and properties.

## 2. Experimental methods

AM samples were built using a Liburdi LAWS 1000 automated deposition system. The robot is controlled by WinLAWS; an in-house software allowing the operator to program axes movements along with defining customized deposition parameters. An IPG Yb:YAG fiber laser reaching up to 1 kW power is used to fuse the material. To prevent excessive oxidation, all deposits are completed in an argon inert environment with oxygen levels below 60 ppm.

Wrought Ti-6Al-4V plates are used as substrates. A Ti-6Al-4V wire spool with Extra-Low Interstitials (Oxygen weight percentage being below 0.13%), manufactured by Lancaster Alloys Company Inc., is used to deposit the material. Single stringers are deposited layer after layer on top of the substrate. Two travel speeds are used in this study: 1.4 mm/s and 7.2 mm/s. A predefined increment of 0.660 mm was set between each deposited pass along the buildup direction. Deposited material is characterized by a thickness of about 2.5 mm. Dimensions of the deposits changed in order to accommodate the extraction of tensile specimens. Printed plates are subsequently used for structure characterization and mechanical properties evaluation.

Macrostructure, microstructure and fractographs were observed

using a Nikon light optical microscope equipped with a Clemex vision system, a Hitachi SU-8230 cold field FE-SEM and a Hitachi SU-3500 cold field FE-SEM.

Phase composition was investigated using a Bruker D8 Discovery X-Ray Diffractometer with a copper source for XRD analysis and a FlatQuad X-Max SDD EDS detector from Bruker assembled with the Hitachi SU-8230 for the chemical element distribution.

Structure evaluations were conducted in two different areas: The top region, associated with a transitional region, where each of the deposited layers did not experience the same thermal history and where structure development is still affected by the process. And the steady state region defined by cyclic macroscopic features usually associated with the same thermal history but where some of the deposited layers may still have experienced a different one.

All samples are extracted in a plane containing both the travel and buildup directions. Flat samples combining the top region and the steady state region are mounted in Bakelite. These samples were ground up to 1200 SiC grit, followed by polishing with 3  $\mu$ m and 1  $\mu$ m diamond suspension and a finish with 0.05  $\mu$ m colloidal silica. Grinding and polishing were done using a Buhler Ecomet-3 autopolisher equipped with an Automet-2 head. These samples were used as is for XRD analysis. A Kroll's Reagent etchant with 91% deionized water ( $H_2O$ ), 6% nitric acid ( $HNO_3$ ) and 3% hydrofluoric acid (HF) was then used on the mounted samples to reveal the structural features using the optical microscope or the SEM.

The previous flat specimens were then ground to a thickness of about 150  $\mu$ m with a 1200 SiC grit finish on both sides. 3 mm disks were punched out from top and steady state regions. Final thinning of the disks was done using a Struers TenuPol-5 automatic electrolytic thinning unit set at 25 V and using a solution consisting of 95% methanol ( $CH_3OH$ ) and 5% sulfuric acid ( $H_2SO_4$ ) cooled at  $-25^\circ C$ . These thin samples were used for STEM characterization and EDS mapping.

A stress relief (SR) cycle according to AMS2801 standard was performed to reduce the residual stresses while keeping the effect of deposition parameters on the developed structure.

The Vickers hardness was measured by means of a Clark Microhardness (CM-100AT) indenter, using a 100 g load. A minimum of 25 measurements was done along the build direction for each of the reported values.

Machined samples proportional to the ASTM E8 standard with a thickness of 0.5 mm, a gage width of 2.5 mm and a gage length of 4.7 mm were extracted in the as-built condition to prevent excessive distortion. Machined subsize specimens meeting ASTM E8 requirements with a thickness of 1.4 mm, a gage width of 6.35 mm and a gage length of 25.4 mm have been extracted for SR condition. Numbers of samples tested in each condition are summarized in Table 1. Heat treated samples were tested at room temperature with a crosshead speed of 2.54 mm/min until fracture using a United SFM-20 kN load frame equipped with a calibrated load cell and an extensometer. Finally, average values of wrought tensile properties produced from five specimens extracted from the base plate and reproducing the subsize specimen geometry previously described have been used to normalize all the results.

**Table 1**  
Number of static tensile samples tested per condition.

Travel speed:	1.4 mm/s		7.2 mm/s	
	X	Z	X	Z
AB	3	3	3	3
SR	3	5	4	4

### 3. Results and discussion

#### 3.1. Effect of travel speed on thermal history

Xu et al. [40] have shown that Ti-6Al-4V strength is following a Hall-Petch type of relationship when using the  $\alpha$  lath thickness as variable. A finer structure develops higher strength, which is usually occurring at the expense of elongation. The main objective behind studying the effect of travel speed is to find a good balance between the two properties.

A critical deposition parameter that substantially affects structure development is the cooling rate  $\dot{T}$ . A higher cooling rate generates a finer structural development [41,42]. Eq. (1) defines cooling rate as:

$$\dot{T} = Gv \tag{1}$$

where  $G$  is the thermal gradient and  $v$  is the growth rate.

Knowing that  $v$  is proportional to the travel speed  $V$  in continuous process [42], the increase in travel speed increases the cooling rates experienced by the deposit and may favor the development of a fine martensitic structure in the last deposited bead

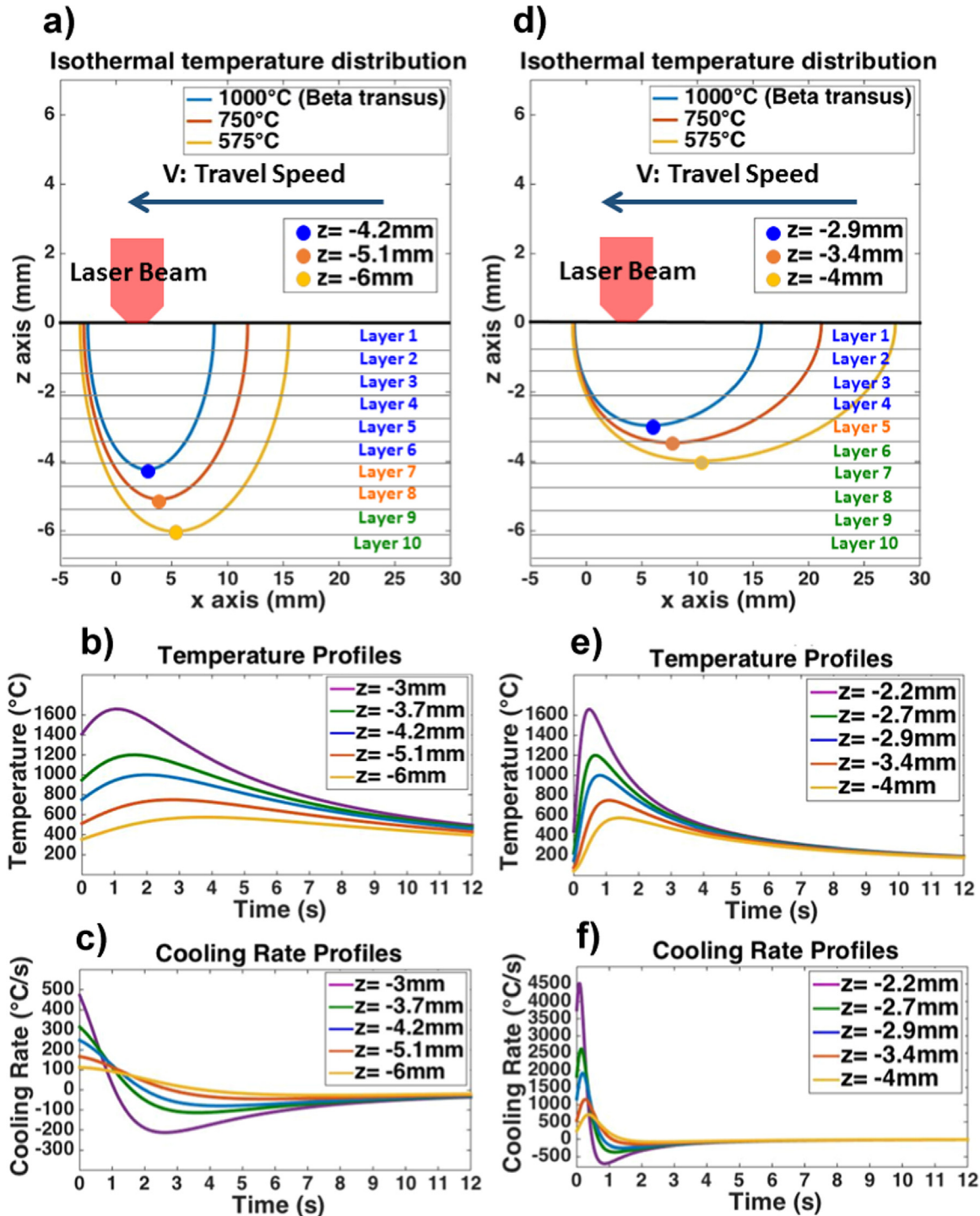


Fig. 1. Isothermal temperature distribution, temperature profiles and cooling rates at 1.4 mm/s in a), b) and c) respectively, and at 7.2 mm/s in d), e) and f) respectively.

The thermal cycle induced for both of the selected travel speeds were predicted by using a simple 3D Rosenthal equation defined in Eq. (2):

$$\frac{2\pi(T - T_0)kr}{Q} = \exp\left(\frac{-V(r - x)}{2\alpha}\right) \quad (2)$$

where  $T$  is the temperature,  $T_0$  the workpiece temperature,  $k$  the thermal conductivity,  $\alpha$  the thermal diffusivity,  $V$  the travel speed,  $Q$  the laser power and  $r$  the radial distance.

Fig. 1 presents isothermals, temperature profiles and cooling rates predicted for both travel speeds. A travel speed of 1.4 mm/s develops more of the circular isothermal shapes as depicted in Fig. 1(a), characteristic of slower travel speeds [42], as opposed to the tear drop shape in Fig. 1(d) developed by the travel speed set at 7.2 mm/s [42]. This last condition induces steeper temperature profiles as shown in Fig. 1(e) that yield to higher cooling rates shown in Fig. 1(f). As it can be seen in Fig. 1(f), some of the cooling rates exceed the theoretical critical rate of full martensitic formation set at 410 °C/s [13] as opposed to the cooling rates achieved by a lower travel speed depicted in Fig. 1(c).

Apart from the qualitative observations on the melt pool shape, Fig. 1(a) and (b) also provide a theoretical quantitative result on the number of layers affected by a predefined isothermal. Three critical isothermals have been computed for both travel speeds: the  $\beta$  transus isothermal set at 1000 °C where the allotropic transformation takes place, the 750 °C isothermal above which microstructure coarsening still takes place [43,44] and a last isothermal associated with a typical aging temperature set at 575 °C. Theoretical deposited layers based on the laser head increment of 0.660 mm along the buildup direction have also been displayed.

From these isothermals, two theoretical distinct regions can be identified for both travel speeds. First, the top region defined by the area that was affected by temperatures exceeding 750 °C. This region is characterized by microstructural changes such as liquid and solid phase transformations and grain coarsening during the deposition process. The width of that region can be assessed by the lowest point on the 750 °C isothermal. A travel speed of 1.4 mm/s exhibits a larger region with a width of 5.1 mm as opposed to 3.4 mm for the faster travel speed. Approximately 8 and 5 layers respectively are thermally affected in this region. Then, temperatures below 750 °C do not allow any substantial structural changes. This is the second region that is referred to as the steady state region. Temperatures still reach aging temperatures though, allowing some rearrangement of crystallographic defects such as linear dislocations for instance [45,46]. It is finally interesting to note that the lowest point of an isothermal is not necessary aligned with the physical representation of the deposited layers. Definition of these regions is as a consequence independent of the layer geometry also reported by Baufeld et al. [31].

### 3.2. Structure evaluation

#### 3.2.1. Macrostructure

Columnar prior  $\beta$  grains are observed at both travel speeds. Larger grains with a width of  $2.5 \text{ mm} \pm 1.4 \text{ mm}$  developed at 1.4 mm/s, as shown in Fig. 2(a). The faster travel speed developed thinner columnar prior  $\beta$  grains with a width of  $1.3 \text{ mm} \pm 0.7 \text{ mm}$ , as shown in Fig. 2(b). A similar observation has been provided by Brandl et al. [16].

Another typical observation associated with Ti-6Al-4V deposits is the presence of bands, as highlighted in Fig. 2(a) and (b). These bands are developed through the successive thermal cycles that underwent one layer by the deposition of the subsequent layers. It was often reported in the literature that this visual effect is due to a change in  $\alpha$  platelets arrangements changing from colony in the bands to  $\alpha + \beta$  basket weave in between [7,47]. This was also observed in the present study. Spacing between each couple of bands was measured at about 0.650 mm. This corresponds well to the predefined laser head

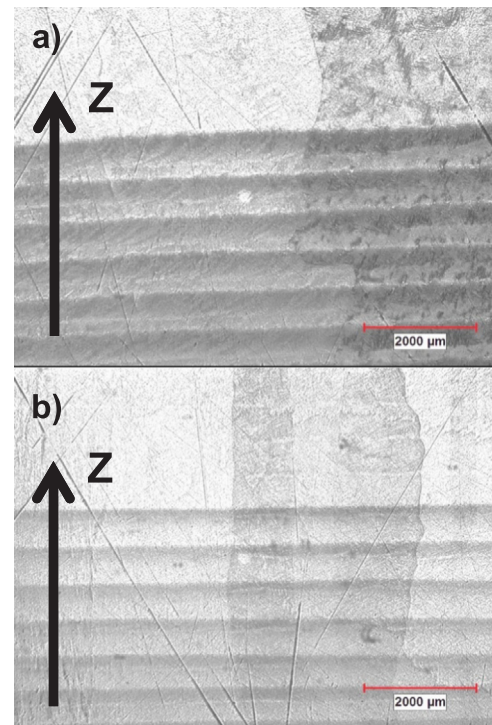


Fig. 2. a) Macrostructures at  $1.4 \text{ mm s}^{-1}$  and b) at  $7.2 \text{ mm s}^{-1}$ .

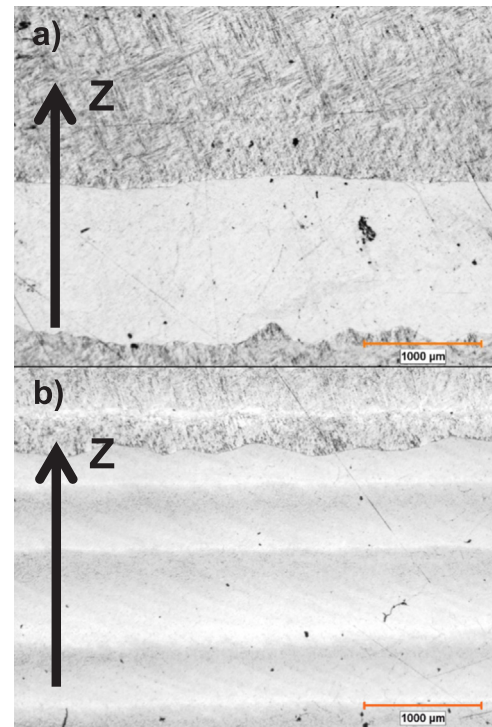
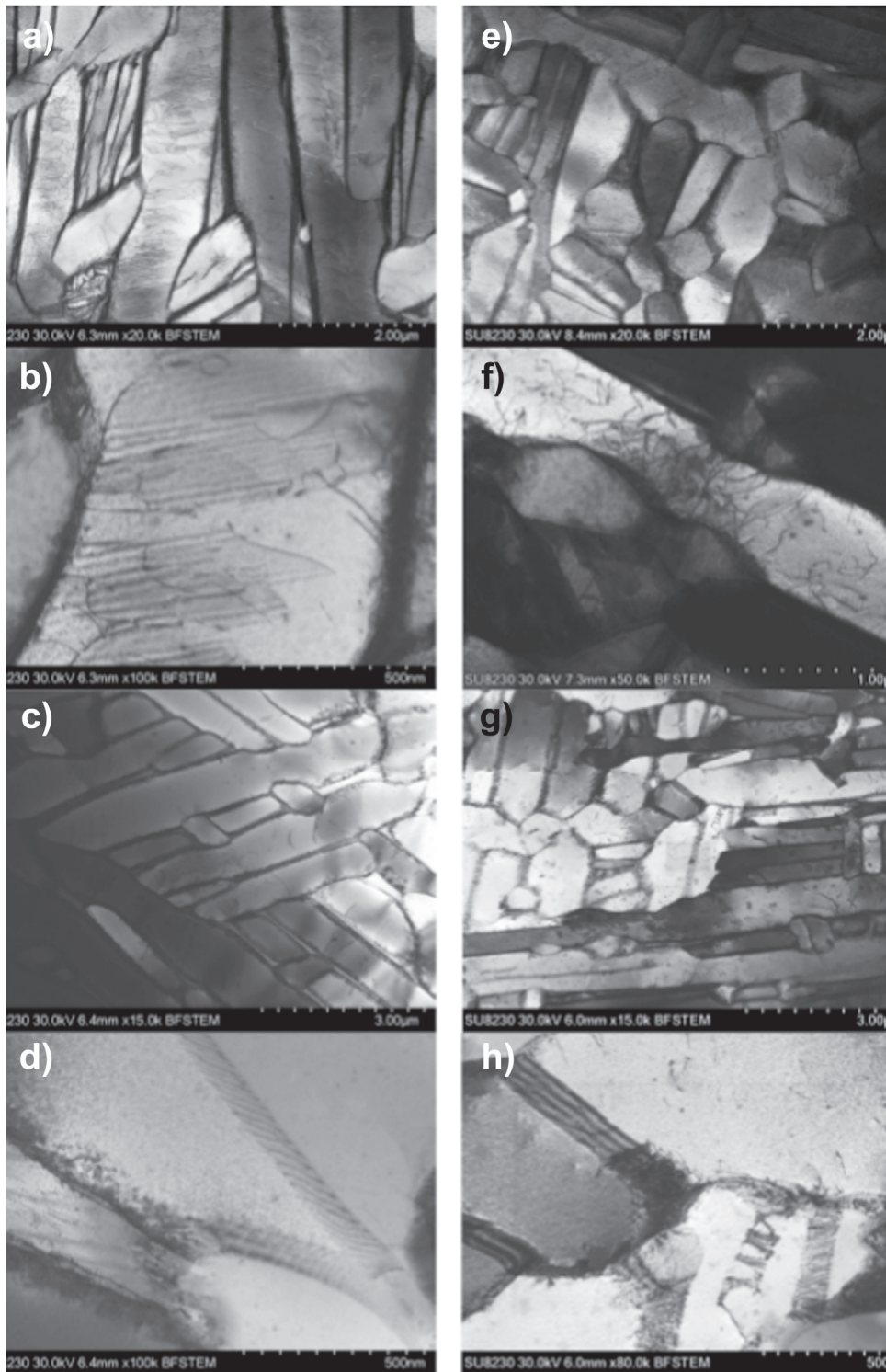


Fig. 3. Horizontal prior  $\beta$  grains developed at 1.4 mm/s in the a) top region and b) the steady state region.

increment of 0.660 mm.

The upper region is then characterized by the absence of these bands as observed in Fig. 2. A travel speed of 1.4 mm/s exhibited a larger region that was experimentally measured at about 4.5 mm, whereas a region of about 2.8 mm has been measured on the samples built at 7.2 mm/s. It is assumed that bands are formed once the induced temperature in the part is low enough to prevent the formation of  $\alpha$



**Fig. 4.** STEM micrographs of the top region for samples processed at a), b) 1.4 mm/s and e), f) 7.2 mm/s and of the steady state region for samples processed at c), d) 1.4 mm/s and g), h) 7.2 mm/s.

colonies. This temperature was reported as being below the limit set at the  $\beta$  transus temperature [31,33]. Overall, the computed regions in Section 3.1 closely match the experimental observations.

Due to their cyclic property, the previously described bands are often associated by extension with the steady state region defined in the previous section [7,31,47]. This will be the case in this study. As a consequence, the upper region is associated with the top region. In this case, the top region does not take into account the possible coarsening

effect for temperatures comprised between the 750 °C and the 1000 °C isothermals.

A key observation on the developed prior  $\beta$  grain morphology is shown in Fig. 3. Indeed, a travel speed of 1.4 mm/s enabled the recrystallization of the columnar prior  $\beta$  grains into horizontal prior  $\beta$  grains at both the top and steady state regions and averaging  $2.2 \text{ mm} \pm 1.4 \text{ mm}$  in width. It is believed that these prior  $\beta$  grains are the result of an accumulation of residual stresses combined with the

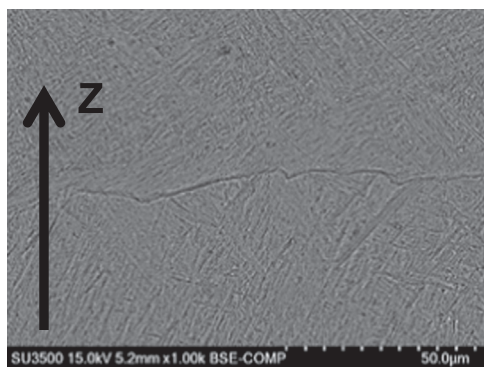


Fig. 5. Grain boundary allotriomorph  $\alpha_{GB}$  and  $\beta$  colonies observed at the horizontal prior  $\beta$  grain boundary developed at 1.4 mm/s.

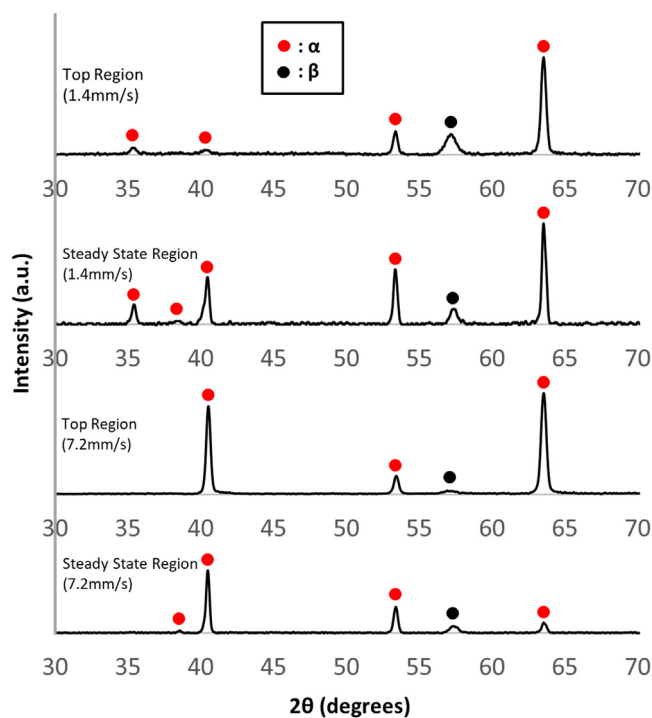


Fig. 6. XRD patterns of the top and steady state regions at 1.4 mm/s and 7.2 mm/s.

subsequent re-heat in the  $\beta$  phase field from the deposition of the subsequent layers. This is in agreement with the larger top region that developed at 1.4 mm/s and showing the extent of the regions that went through temperatures exceeding the  $\beta$  transus temperature. Combining this information, with the computed temperature profiles and cooling rates in the previous section, recrystallization of the prior beta grains is enabled in theory when the region remains in the  $\beta$  field temperature for more than 5 s and associated to cooling rates comprised between 240 °C/s to 475 °C/s. To the best of our knowledge, this is the first time that such a phenomenon has been reported in the as-built condition. Dinda et al. [21] reported a similar observation following a post deposition heat treatment above the  $\beta$  transus temperature at 1050 °C for 1 h followed by either air cooling or furnace cooling. On the other hand, a travel speed of 7.2 mm/s samples did not exhibit any recrystallization of the columnar prior beta grains. This is in agreement with the smaller top region that developed in this condition. This region remaining less than 2 s in the  $\beta$  field temperature and exhibiting larger cooling rates exceeding in theory 1900 °C/s as computed in the previous section.

### 3.2.2. As-built microstructures

Microstructural analysis in the as-built condition has first been investigated using STEM micrographs as shown in Fig. 4.

The  $\alpha$  platelet thickness measured for the top regions were assessed to about 614 nm  $\pm$  150 nm at 1.4 mm/s which is equivalent to the results derived by Baufeld et al. [7] using the LWD or the SMD processes. At 7.2 mm/s, the width of the alpha platelets decreased to 335 nm  $\pm$  113 nm which is closer to what can be produced by powder bed processes such as described by Xu et al. [40]. This is in agreement with experienced higher cooling rates by the deposits. Moreover, these regions show the presence of multiple structural defects at both travel speeds, mainly stacking faults contained in  $\alpha$  platelets as shown in Fig. 4(b), and dislocation networks, depicted in Fig. 4(f). Some  $\alpha$  platelets have also shown the presence of twins. Twinning in the hcp  $\alpha$  phase is inherent to a deformation mechanism. It has been widely reported that twinning can account as an additional deformation mechanism to a mechanical load when the stress is applied along the hexagonal c-axis [48–57]. Twinning however as a pure mechanical deformation mechanism has been reported to be non-existent when exposed to low strain rates and to temperatures above room temperature while weight percentage of aluminum exceeds 5% [57,58]. But twinning activity in the Ti-6Al-4V  $\alpha$  phase has already been reported at high temperatures when high strain rates are present. It is however usually associated with a strong directional texture for the  $\alpha$  phase [52]. Which is usually not the case for DED processes mostly associated with a nearly random texture of the  $\alpha$  phase [59–61]. Twinning, stacking faults and dislocation networks have also been reported to be present in the Ti-6Al-4V hcp  $\alpha'$  phase during martensitic transformation, experimentally [13,21,57,62,63] and by computer simulation [64,65]. The non-diffusional transformation process that characterizes martensitic transformation follows the Invariant Plane Strain (IPS) condition [66]. This condition states that there is at least one undistorted crystallographic plane shared between the martensitic phase and the parent lattice where all the crystallographic directions remain coherent. The Bain strain induced by the lattice strain during the bcc to hcp transformation does not satisfy alone the IPS. An additional strain component, namely the Lattice Invariant Shear (LIS) has thus been introduced. The LIS introduces a new strain component by dislocation slip, stacking faults formation or twinning that adds to the Bain strain in order to satisfy the IPS [62,63,66]. As martensitic transformation in Ti-6Al-4V can occur for cooling rates above 20 °C/s [13], observations made in Fig. 4(b) and (f) are in line with the presence of martensite in the top regions of both travel speeds.

Additionally, coarsening of the  $\alpha$  platelets induced by the repeated thermal cycles due to the deposition of subsequent layers has been observed at both travel speeds within the steady state regions. As expected, the slower travel speed deposit exhibited a greater coarsening reaching 859 nm  $\pm$  178 nm as more deposited layers are thermally affected by the addition of a layer as shown in Fig. 1(a) and (d). This is in agreement with the typical values reported within the steady state regions of LWD processes or SMD processes [7,31]. The  $\alpha$  platelets produced at 7.2 mm/s coarsened to 436 nm  $\pm$  116 nm as fewer layers were thermally affected which is slightly better than what can be produced by common LPD processes reaching about 650 nm in average [21,25]. Main structural defects such as stacking faults and twins have not been observed in these regions. On the opposite, multiple arrays of dislocations have been observed at the  $\alpha$  platelets boundaries such as depicted in Fig. 4(d) and (h). These features are characteristic of a diffusion-controlled transformation process from the bcc  $\beta$  phase to the hcp  $\alpha$  phase [66]. In this scenario, and as opposed to the martensitic IPS condition, only one crystallographic direction remains invariant in the bcc to hcp transformation. This crystallographic direction is also usually associated with equispaced dislocations that lie on the shared crystallographic plane between the  $\alpha$  platelet and the parent lattice. Some  $\alpha$  platelets show signs of semi coherent boundaries that contain structural ledges and dislocations as seen in Fig. 4(h). These were again

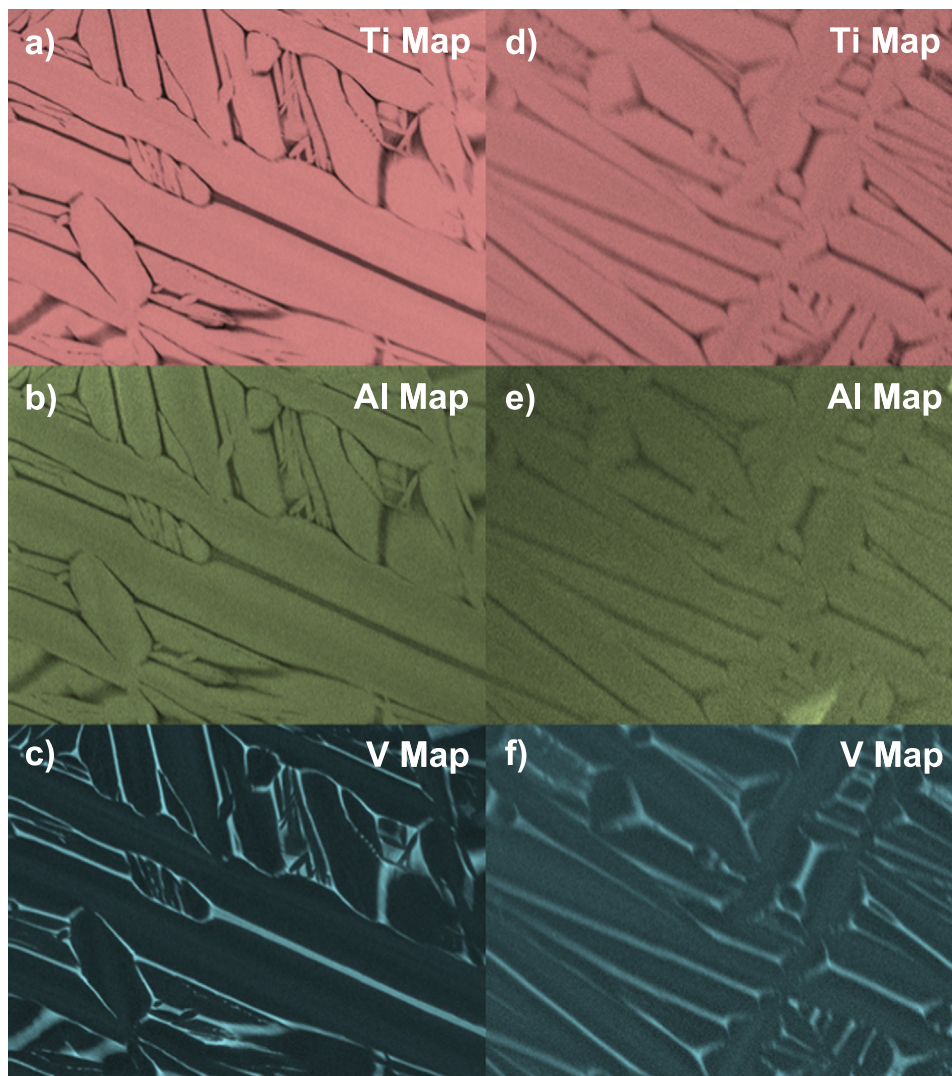


Fig. 7. EDS maps showing distribution of titanium, aluminum and vanadium in the top region for the sample built at 1.4 mm/s in a), b) and c) respectively, and for the sample built at 7.2 mm/s in d), e) and f) respectively.

documented as being characteristic of diffusional transformations of the bcc  $\beta$  phase to hcp  $\alpha$  phase [66,67]. All these observations are in agreement with slower cooling rates experienced during the last allotropic transformation and the subsequent heat treatments in the  $\alpha + \beta$  range experienced by the deposited layers in the steady state regions.

Recrystallization of prior  $\beta$  grains at 1.4 mm/s observed in the previous section is associated with the development of long  $\alpha$  grains along the prior  $\beta$  grains boundaries, as shown in Fig. 5. Grain boundary allotriomorphs  $\alpha_{GB}$  are associated with a diffusional process that takes place during slow cooling [66,68–70]. This is reported as the first feature to develop during the allotropic transformation. Misorientation at the grain boundary of the two prior  $\beta$  grains provides preferential nucleation sites for  $\alpha_{GB}$  and favors their growth.  $\alpha_{GB}$  following the Burgers orientation relationship with at least one of the two prior  $\beta$  grains while minimizing the mismatch with the other one. Colonies of  $\alpha$  platelets have also been observed starting from the  $\alpha_{GB}$  and extending from either side of the adjacent prior  $\beta$  grains. This is typically reported as being the second diffusional feature that takes place during slow cooling. Nucleation and growth mechanisms of  $\alpha$  colonies are still unclear as of today. Two recurrent hypotheses are usually encountered to explain the precipitation of  $\alpha$  colonies: sympathetic nucleation [66,68] and interface instability [66,69,70], both induced at the grain boundary allotriomorphs. Bhattacharyya et al. [71] showed then that their

growth direction depends essentially on the initial misorientation of the prior  $\beta$  grains. Finally, upon subsequent cooling, high undercooling is reached leading to the development of an  $\alpha + \beta$  basket weave type of structure in the rest of the prior  $\beta$  grain.

Fig. 6 shows the XRD patterns indicating the presence of the  $\beta$  phase in top and steady state regions of samples processed at 1.4 mm/s. This shows that cooling rates experienced by these allow the diffusional growth of  $\alpha$  platelets within the  $\beta$  matrix. This is in agreement with the theoretical study of the experienced cooling rates as shown in Fig. 1(c). A small fraction of the microstructure in the top region can still be of the martensitic phase as observed previously with the STEM characterization. This is in agreement with the observations made by Ahmed et al. [13] that suggests that martensite can still develop for cooling rates comprised between 20 °C/s and 410 °C/s. The absence of a strong peak of intensity at the top region of the samples processed at 7.2 mm/s suggests that most of the microstructure developed in Fig. 4(e) and (f) is a mix of  $\alpha'$  and  $\alpha$  phases with traces of the  $\beta$  phase. This implies that cooling rates are not fully exceeding the theoretical threshold of 410 °C/s for producing a complete martensitic structure. This again matches with the graph presented in Fig. 1(f). Deposition of subsequent layers provides then enough energy to transform the previously developed martensitic structure by precipitating the  $\beta$  phase along the  $\alpha$  platelets boundaries. This is observed by the presence of the

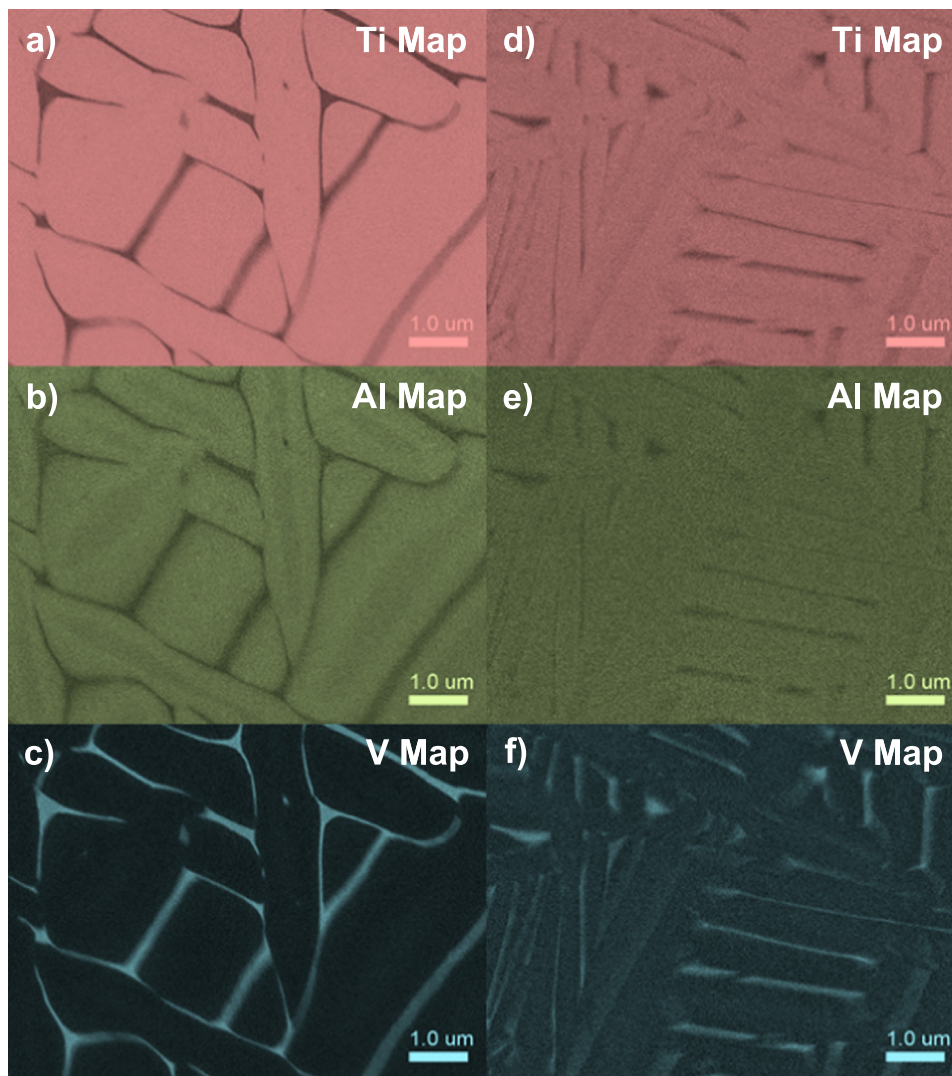


**Fig. 8.** EDS maps showing distribution of titanium, aluminum and vanadium in the steady state region for the sample built at 1.4 mm/s in a), b) and c) respectively, and for the sample built at 7.2 mm/s in d), e) and f) respectively.

clear  $\beta$  peak at the steady state region.

EDS maps were generated in Figs. 7 and 8 using a novel technique introduced by Brodusch et al. [72]. Indeed, these maps were processed using the f-ratio method that provide relevant qualitative results in terms of distribution of the principal chemical elements namely titanium, aluminum and vanadium. This method was successful in removing diffraction related features such as introduced by the dislocation network that could induce erroneous interpretations. This is extremely useful in order to identify the distribution of each of the  $\alpha$  and  $\beta$  phases associated with the segregation of their respective stabilizing elements. As expected, aluminum is found in higher concentration within the  $\alpha$  platelets. Vanadium on the other hand stabilizes the  $\beta$  phase and is mainly concentrated along the  $\alpha$  platelets boundaries. Moreover, segregation of vanadium along the  $\alpha$  platelets boundaries in the top region of the samples built at 7.2 mm/s as seen in Fig. 7(f) suggests again the presence of the  $\beta$  phase as detected by the XRD investigations. The more continuous distribution of the  $\beta$  phase at 1.4 mm/s as observed in Figs. 7(c) and 8(c) is in agreement with the experienced slower cooling rates.

### 3.2.3. Stress relieved microstructures

Fig. 9 shows some typical micrographs of the stress-relieved samples at both travel speeds. Macroscopic features presented in Section 3.2.1

and induced by the choice of deposition parameters and the cyclic property of the deposition of additional layers such as the columnar or horizontal prior  $\beta$  grains and the presence of bands are still observable as shown in Fig. 9(a) and (b).

The morphology of the  $\alpha$  platelets did not drastically change. Thickness of  $\alpha$  platelets is still in the same size range being at  $812 \text{ nm} \pm 169 \text{ nm}$  and  $538 \text{ nm} \pm 143 \text{ nm}$  for samples processed at 1.4 mm/s and 7.2 mm/s respectively. As pointed out by Appolaire et al. [68] and shown in Ref. [73], a typical ternary Ti-Al-V phase diagram in the temperature range of the stress relief heat treatment shows a more pronounced curvature for the  $\beta$  phase field boundary when compared with the one developed for the  $\alpha$  phase field. In other words, a larger variation of the chemical elements can occur preferentially within the  $\beta$  phase during a stress relief heat treatment. Knowing also that the concentration of  $\alpha$  stabilizing elements at the  $\alpha$  platelet boundary is inversely proportional to the grain curvature [70], it is safe to assume that a gradient in the stabilizing chemical elements of both phases exist at the boundary post deposition. The smaller the curvature, the better stabilized will the  $\alpha$  phase be at the tip. The EDS maps of the steady state regions produced in the as built condition as shown in Fig. 8 is in agreement with the last statement. Indeed, the faster travel speed condition developed finer  $\alpha$  platelets and it can be seen that a higher aluminum concentration is found at the tip of the  $\alpha$  platelets as shown

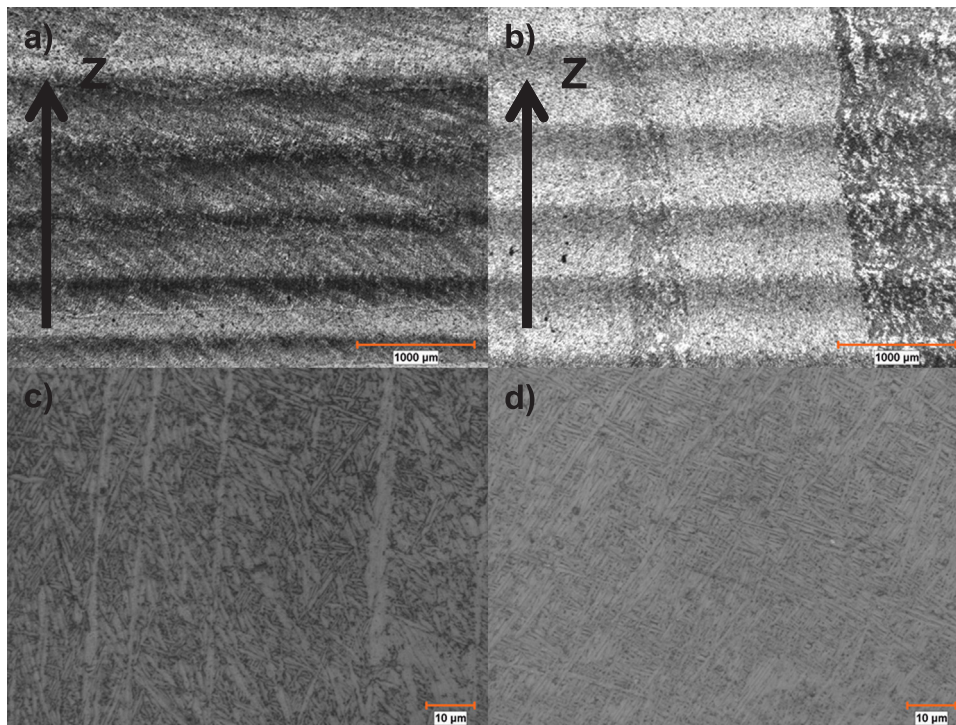


Fig. 9. Micrographs of stress-relieved samples following AMS2801 standard and furnace cooled, at 1.4 mm/s a) and c) and at 7.2 mm/s b) and d).

in Fig. 8(e) almost preventing any precipitation of vanadium in these areas as shown in Fig. 8(f). As opposed to the samples built at 1.4 mm/s that developed larger platelets and where we can see an almost even distribution of the vanadium along the platelets boundaries as depicted in Fig. 8(c). Stress relieving is believed then to provide enough energy to precipitate the  $\beta$  phase along the  $\alpha$  platelets tips and approach an equilibrium state depicted by the ternary diagram [73]. Being easier to check that hypothesis with samples produced at 7.2 mm/s, new EDS maps of the steady state region have been acquired for the stress-relieved condition as shown in Fig. 10 and using again the *f*-ratio method introduced by Brodusch et al. [72]. Signs of precipitation of the  $\beta$  phase are to a moderate extent confirmed by the presence of a higher concentration of vanadium at the  $\alpha$  platelets tips as some of them are circled in red in Fig. 10(c).

### 3.3. Mechanical properties

#### 3.3.1. As-built static tensile properties

As opposed to strength when the gage cross section is kept constant, elongation is affected by the specimen geometry. In general, elongation is proportional to the  $L/A^{1/2}$  ratio where *L* is the original gage length of the tensile sample and *A* the corresponding initial cross section as stated by the ASTM E8 specification and suggested by Simonelli et al. [60]. Usually, the smaller the ratio the higher the elongation. Variation of elongation in this case is typically nonlinear [74]. On the opposite, the larger the ratio the lower the elongation. In this case, elongation usually stabilizes around a fixed value [74]. As a consequence of this variability in elongation, only strength results in the as-built condition were presented in Table 2. The statistically equivalent results developed in the X and Z directions for both travel speeds show that strength exhibit an isotropic behavior. The finer microstructure developed at 7.2 mm/s produced higher strengths equivalent to the typical wrought properties used to normalize the results. These were consistently exceeding the minimum wrought requirements as set by the AMS4911 specification. Lower cooling rates induced at 1.4 mm/s developed lower strengths hardly meeting the same minimum requirements but consistently exceeding the DED minimum requirements as set by the AMS4999

specification.

The beneficial effect of the finer microstructure can be explained in terms of heat input associated to both travel speed. Indeed, these heat inputs were compared to the typical heat inputs developed by the different DED processes available in the literature as shown in Fig. 11. It can be seen that the heat input developed at 7.2 mm/s is equivalent to the typical heat input developed by LPD processes [8,22,25]. This can explain in turn the higher strength developed in this condition. As opposed to the slower travel speed set at 1.4 mm/s that is more comparable to the typical heat input associated to LWD or SMD processes and associated to a coarser microstructure [7,15,33].

#### 3.3.2. Stress-relieved static tensile properties

Major structural features that developed post-deposition were mostly preserved post-stress-relief heat treatment as reported in Section 3.2.3. Generated tensile results are summarized in Table 3. These results show only a slight decrease in the average strength but remain above the respective AMS minimum requirements when compared with the results developed in the as-built condition. Results in strength are still isotropic. A strong anisotropy in elongation is observed though at 1.4 mm/s with a higher elongation measured along the X direction. Samples built at 1.4 mm/s exhibited slower cooling rates during the deposition process that favored the development of grain boundary allotriomorphs and colonies of  $\alpha$  platelets known to be detrimental for the generated tensile properties [7–9,15,32,75]. Recrystallization of columnar prior  $\beta$  grains into horizontal prior  $\beta$  grains has also been observed. As a consequence, samples built at 1.4 mm/s in this study exhibited an anisotropy in elongation along the Z direction which is at the opposite of the typical anisotropy reported in the literature [7–9,15,32,75]. In this case, elongation exceeds minimum DED requirements along the X direction but does not meet any of the AMS or ASTM specifications along the Z direction. Generated elongations were statistically equivalent in both the X and Z directions at 7.2 mm/s and consistently exceeding the minimum wrought requirements in the Z direction while meeting in average the same requirements in the X direction. These samples experienced faster cooling rates reducing the development of the detrimental microstructural features and resulting

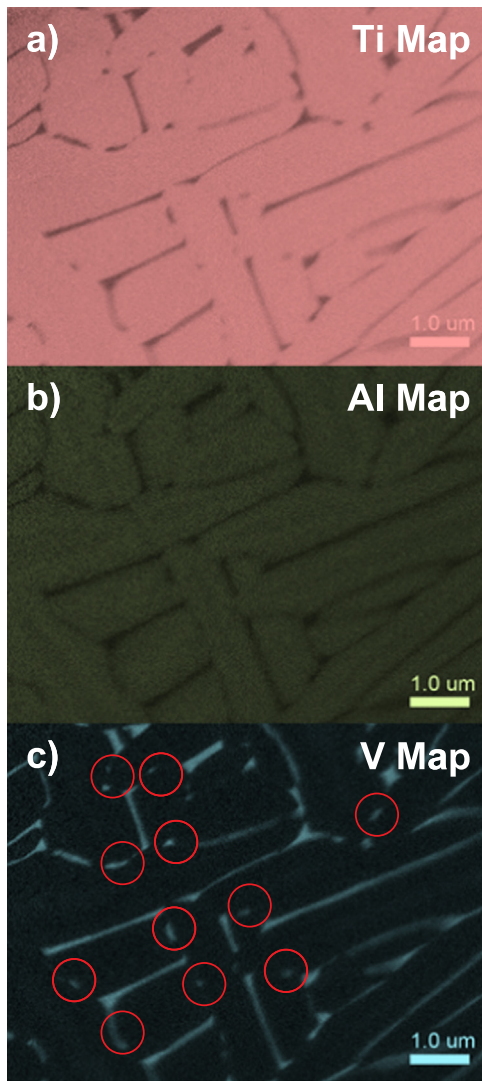


**Fig. 10.** EDS maps of a stress relieved sample following AMS2801 standard processed at 7.2 mm/s and furnace cooled showing the distribution of a) titanium, b) aluminum and c) vanadium in the steady state region.

**Table 2**  
Room temperature static tensile properties of the as-built specimens.

Travel speed (mm/s)	Tensile direction	Yield strength ((MPa/MPa) * 100)	Ultimate tensile strength ((MPa/MPa) * 100)
1.4	X	86.5 < <b>87.5</b> < 89.5, 1.7	83.3 < <b>87.0</b> < 88.4, 2.3
	Z	83.9 < <b>90.0</b> < 94.1, 5.3	84.5 < <b>88.3</b> < 91.2, 3.4
7.2	X	102.2 < <b>103.4</b> < 105.4, 1.7	99.5 < <b>100.1</b> < 100.6, 0.6
	Z	98.7 < <b>103.5</b> < 107.3, 4.4	102.6 < <b>103.4</b> < 103.7, 0.5

Results are presented as:  $\sigma_{min} < \bar{\sigma} < \sigma_{max} \pm SD$  where  $\sigma_{min}$  is the lowest value,  $\bar{\sigma}$  the mean value,  $\sigma_{max}$  the highest value and  $SD$  the standard deviation from the mean value.

in enhanced static tensile properties. In this case a similar observation on the effect of faster cooling rates on the developed microstructure was provided by Åkerfeldt et al. [75].

Generated results in the as-built and stress relieved conditions were next compared to typical results generated by different DED processes and found in the literature as shown in Fig. 12. Results in strength for the samples processed at 7.2 mm/s are similar to the ones developed

with LPD for which typical average strength exceed 940 MPa in yield strength and 1040 MPa in ultimate tensile strength. This is in contrast with the samples processed at 1.4 mm/s that developed equivalent results to the one typically reported using LWD or SMD. When taking each process individually, a stress relief cycle does not seem to affect strength properties as opposed to elongation that appears to decrease in average.

### 3.3.3. Fracture mechanisms

Fracture surfaces presented similar features regardless of the investigated condition. This section summarizes the main results.

First, optical micrographs of the fracture surfaces were generated. Two different fracture profiles developed when testing the samples orthogonal to the columnar prior  $\beta$  grains. Samples built at 1.4 mm/s were mainly characterized by an intergranular type of fracture as shown in Fig. 13(a) and characterized by a linear fracture profile. A combination of intergranular and transgranular fracture modes may occur for samples processed at 7.2 mm/s. In this case, fracture profiles are roughly inclined with a  $\pm 45^\circ$  angle when measured with respect to the loading direction. Evidence of transgranular fracture was observed when tested along the columnar prior  $\beta$  grain as shown in Fig. 13(b). Crack propagation tends to happen along grain boundary allotriomorphs  $\alpha_{GB}$  as shown in Fig. 13(c) when tested orthogonal to the columnar prior  $\beta$  grains and mostly observed for samples processed at 1.4 mm/s. While microstructure found within the prior  $\beta$  grains tends to drive crack propagation for samples tested along the columnar prior  $\beta$  grains as shown in Fig. 13(d) and characterized by a more serrated fracture path.

SEM fractographs mostly revealed the presence of a healthy population of dimples characteristic of a ductile type of fracture as shown in Fig. 13(e) and (f). Shi et al. [35] suggested that refined population of dimples would lead to higher strength and lower elongation. They also suggested that shallow dimples are associated to lower elongation. Dimples were measured at  $3.4 \mu\text{m} \pm 1.8 \mu\text{m}$  and  $1.8 \mu\text{m} \pm 0.8 \mu\text{m}$  for samples produced at 1.4 mm/s and 7.2 mm/s, respectively. Which is in line with Shi et al. [25] comments regarding the strength. The shallower dimples morphology for the samples processed at 1.4 mm/s as seen in Fig. 13(e) can also account for the lower elongation measured in Table 3. Macrographs of the fracture surfaces at the bottom right corner of Fig. 13(e) and (f) provide an additional information on the amount of necking that samples experienced. Precise measurements were provided in Table 3 in terms of reduction of area. In general, and following a stress relief thermal cycle, samples processed at 7.2 mm/s showed an increased necking activity which is in agreement with the measured higher elongation. In addition, the anisotropy in elongation for samples processed at 1.4 mm/s is associated with a similar behavior in the measured reduction of areas.

### 3.3.4. Hardness

The as-built condition produced statistically equivalent hardness with  $312\text{HV} \pm 11\text{HV}$  and  $327\text{HV} \pm 10\text{HV}$  for samples processed at 1.4 mm/s and 7.2 mm/s, respectively. Strengthening of the deposits have been observed following a stress relief post deposition heat treatment measured at  $334\text{HV} \pm 11\text{HV}$  and  $376\text{HV} \pm 12\text{HV}$  for samples processed at 1.4 mm/s and 7.2 mm/s, respectively. Studies implied that precipitation of  $\text{Ti}_3\text{Al}$  intermetallics might explain this strengthening mechanism [15,18]. However, TEM investigation of the samples – not presented in this study – were not able to support this claim. As  $\alpha$  platelets morphology were not affected by the stress relief, grain boundary strengthening mechanism can also be ruled out. Solid solution strengthening is most likely at the origin of the strengthening observation which is supported at some extent by Brandl et al. through EDX line scan measurements [18]. The higher strengthening measured for samples processed at 7.2 mm/s can then be associated to the finer microstructure developed in this condition. Further investigation on the strengthening mechanisms will be presented in another study.

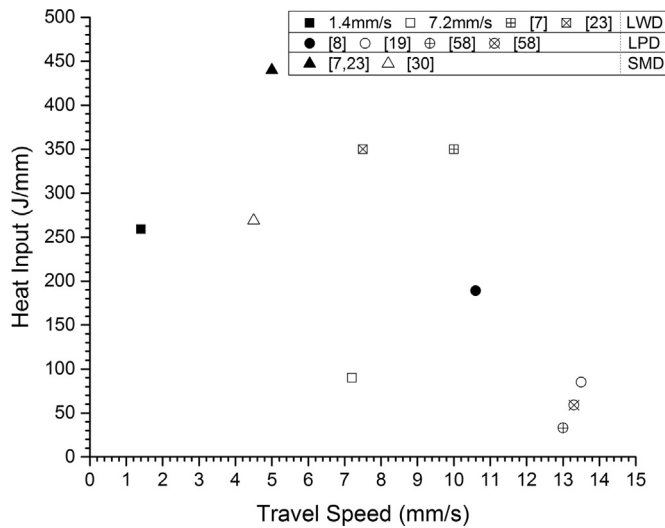


Fig. 11. Developed heat input with respect to travel speeds of different DED processes.

### 4. Conclusion

Effects of travel speed and a stress relief post deposition heat treatment on the developed microstructure and mechanical properties of LWD of thin Ti-6Al-4V samples have been investigated. The following results were found:

A travel speed set at 7.2 mm/s helped in refining the generated microstructure. Thickness of  $\alpha$  platelets were equivalent to the typical thicknesses developed by LPD processes. As a consequence of this developed microstructure, mechanical properties were substantially improved being isotropic and exceeding or meeting minimum wrought requirements as set by the AMS 4911.

A travel speed set at 1.4 mm/s promoted the recrystallization of columnar prior  $\beta$  grains into horizontal prior  $\beta$  grains. Detrimental grain boundary allotriomorphs  $\alpha_{GB}$  developed along the boundaries of recrystallized prior  $\beta$  grains as well as colonies of  $\alpha$  platelets extending in adjacent prior  $\beta$  grains. Thickness of alpha platelets were similar to the typical thicknesses developed by LWD and SMD processes found in the literature. As a consequence lower strength hardly meeting the typical aerospace requirements.

Most of the microstructural features were preserved following a stress relief post deposition heat treatment. Similar trends were then observed for the generated strengths with regard to the selected travel speed. Moreover, strongly anisotropic elongations were developed for samples processed at 1.4 mm/s. Elongation being greater along the X direction. This shows the importance of selecting the optimum deposition parameters at the start of the printing process. Designers that want to use AM as a manufacturing process must also take into account the fact that anisotropy in elongation might be at the opposite of the current common knowledge when deposition parameters enable the recrystallization of prior  $\beta$  grains.

It will be of interest in future studies to keep lowering the heat input

Table 3

Room temperature static tensile properties of the stress relieved specimens.

Travel speed (mm/s)	Tensile direction	Yield strength ((MPa/MPa) * 100)	Ultimate tensile strength ((MPa/MPa) * 100)	Elongation ((%/%) * 100)	Reduction of area (%)
1.4	X	86.3 < 87.2 < 88.7, 1.0	85.0 < 86.1 < 87.7, 1.1	59 < 62 < 66, 3	11.5 < 15.5 < 19.4, 5.6
	Z	82.0 < 85.1 < 87.5, 1.7	82.6 < 85.2 < 87.0, 1.4	15 < 29 < 43, 9	5.9 < 7.7 < 12.5, 3.2
7.2	X	100.2 < 100.5 < 100.7, 0.2	98.7 < 99.0 < 99.3, 0.3	54 < 63 < 83, 12	25.9 < 41.7 < 56.2, 12.4
	Z	93.3 < 95.1 < 97.8, 1.7	93.0 < 96.5 < 100.8, 3.0	69 < 82 < 111, 17	22.7 < 29.7 < 39.4, 7.2

Results are presented as:  $\sigma_{min} < \bar{\sigma} < \sigma_{max}, SD$  where  $\sigma_{min}$  is the lowest value,  $\bar{\sigma}$  the mean value,  $\sigma_{max}$  the highest value and  $SD$  the standard deviation from the mean value.

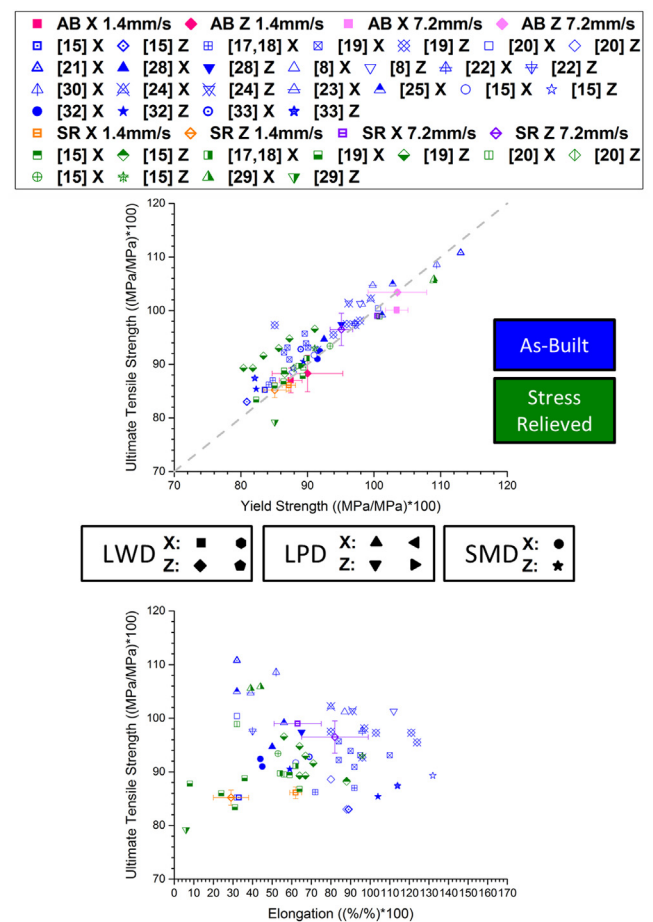
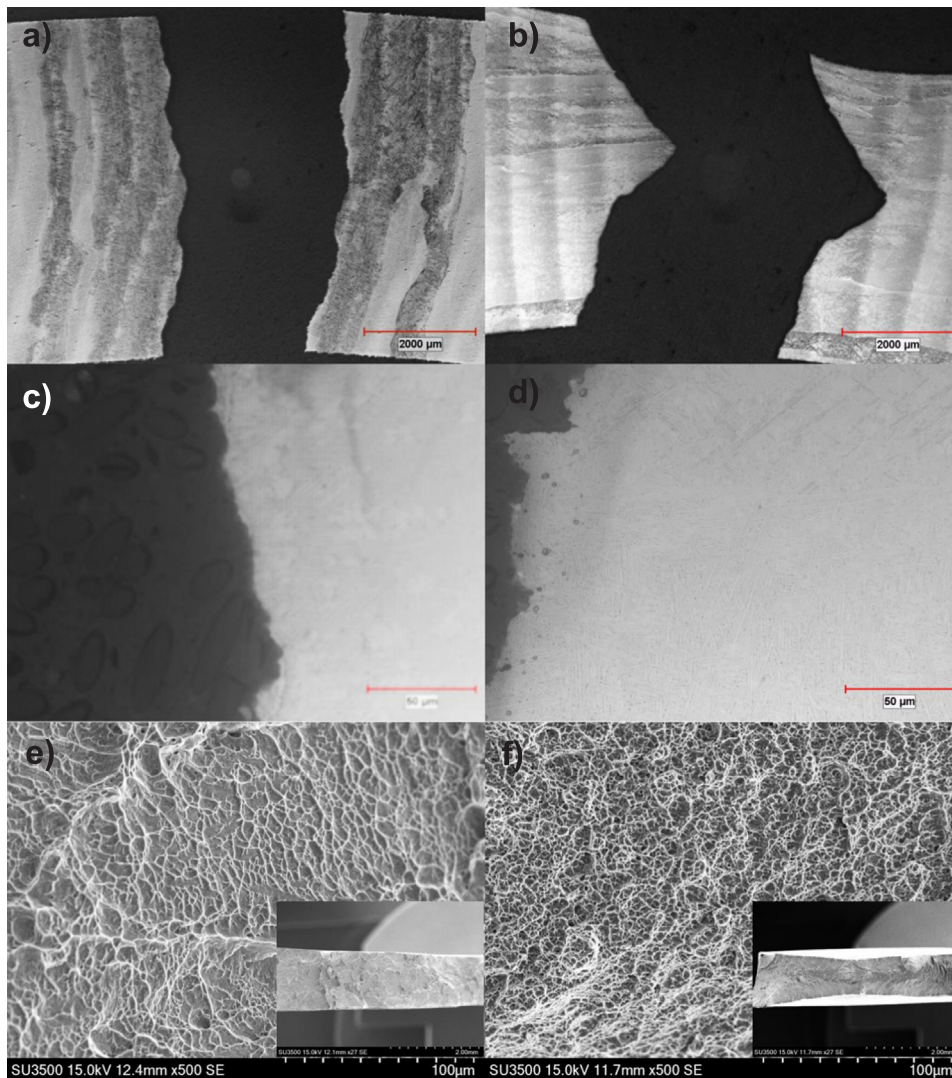


Fig. 12. Investigation of the reported static tensile properties along X or Z at room temperature comparing three different DED processes including LWD, LPD and SMD in the as-built condition in blue and stress relieved in green: a) ultimate tensile strength versus yield strength and b) ultimate tensile strength versus elongation.

associated to LWD while maintaining high cooling rates in order to improve the generated mechanical properties. In-situ monitoring of the deposition process might be one of the keys in achieving this result. It will also be of interest to investigate the effects induced by different post deposition heat treatments with a temperature closer to the  $\beta$  transus temperature.

### Acknowledgments

The authors would like to thank the Consortium de Recherche et d'Innovation en Aérospatiale au Québec (CRIAQ), Liburdi, Centre de Métallurgie du Québec, Bell Helicopter Textron Canada, Bombardier, Edmit, GE, Héroux-Devtek, MDA and Pratt & Whitney Canada for their project contribution under the MANU-601 and NSERC CRDPJ 451386-13 grants.



**Fig. 13.** Optical macrographs of fracture profiles in the stress relieved condition processed and tested in the Z direction processed a) at 1.4 mm/s and b) at 7.2 mm/s and the respective micrographs in c) and d). SEM fractographs in the stress relieved condition and tested in the X direction processed e) at 1.4 mm/s and f) at 7.2 mm/s.

## References

- [1] F.H.S. Froes, M.N. Gungor, M.A. Imam, Cost-affordable titanium: the component fabrication perspective, *JOM* 59/6 (2007) 28–31.
- [2] I. Gibson, D.W. Rosen, B. Stucker, *Additive Manufacturing Technologies Rapid Prototyping to Direct Digital Manufacturing*, Springer, New York, 2010.
- [3] C.K. Chua, K.F. Leong, *3D Printing and Additive Manufacturing Principles and Applications*, 4th edition, World Scientific, Singapore, 2014.
- [4] B. Vandenbroucke, J.-P. Kruth, Selective laser melting of biocompatible metals for rapid manufacturing of medical parts, *Rapid Prototyp. J.* 13/4 (2007) 196–203.
- [5] L. Costa, R. Vilar, Laser powder deposition, *Rapid Prototyp. J.* 15/4 (2009) 264–279.
- [6] T. Vilaro, C. Colin, J.D. Bartout, As-fabricated and heat-treated microstructure of the Ti-6Al-4V alloy processed by selective laser melting, *Metall. Mater. Trans.* 42/10 (2011) 3190–3199.
- [7] B. Baufeld, E. Brandl, O. van der Biest, Wire based additive layer manufacturing: comparison of microstructure and mechanical properties of Ti-6Al-4V components fabricated by laser-beam deposition and shaped metal deposition, *J. Mater. Process. Technol.* 211 (2011) 1146–1158.
- [8] B.E. Carroll, T.A. Palmer, A.M. Beese, Anisotropic tensile behavior of Ti-6Al-4V components fabricated with directed energy deposition additive manufacturing, *Acta Mater.* 87 (2015) 309–320.
- [9] J.S. Keist, T.A. Palmer, Role of geometry on properties of additively manufactured Ti-6Al-4V structures fabricated using laser based directed energy deposition, *Mater. Des.* 106 (2016) 482–494.
- [10] M.J. Donachie, *Titanium: A Technical Guide*, 2nd edition, ASM International, Ohio, 2000.
- [11] C. Leyens, M. Peters, *Titanium and Titanium Alloys. Fundamentals and Applications*, Wiley-VCH, Weinheim, 2003.
- [12] G. Lütjering, J.C. Williams, *Titanium*, Second edition, Springer, New York, 2007.
- [13] T. Ahmed, H.J. Rack, Phase transformations during cooling in  $\alpha + \beta$  titanium alloys, *Mater. Sci. Eng. A* 243 (1998) 206–211.
- [14] S.M. Kelly, S.L. Kampe, Microstructural evolution in laser-deposited multilayer Ti-6Al-4V builds: part I. Microstructural characterization, *Metall. Mater. Trans.* 35A (2004) 1861–1867.
- [15] E. Brandl, B. Baufeld, C. Leyens, R. Gault, Additive manufactured Ti-6Al-4V using welding wire: comparison of laser and arc beam deposition and evaluation with respect to aerospace material specifications, *Phys. Procedia* 5 (2010) 595–606.
- [16] E. Brandl, V. Michailov, B. Viehweger, C. Leyens, Deposition of Ti-6Al-4V using laser and wire, part I: microstructural properties of single beds, *Surf. Coat. Technol.* 206 (2011) 1120–1129.
- [17] E. Brandl, F. Palm, V. Michailov, B. Viehweger, C. Leyens, Mechanical properties of additive manufactured titanium (Ti-6Al-4V) blocks deposited by a solid-state laser and wire, *Mater. Des.* 32 (2011) 4665–4675.
- [18] E. Brandl, A. Schoberth, C. Leyens, Morphology, microstructure, and hardness of titanium (Ti-6Al-4V) blocks deposited by wire-feed additive layer manufacturing (ALM), *Mater. Sci. Eng. A* 532 (2012) 295–307.
- [19] S.H. Mok, G. Bi, J. Folkes, I. Pashby, J. Segal, Deposition of Ti-6Al-4V using a high power diode laser and wire, part II: investigation on the mechanical properties, *Surf. Coat. Technol.* 202 (2008) 4613–4619.
- [20] E. Brandl, C. Leyens, C.D. Donne, et al., Deposition of Ti-6Al-4V using Nd:YAG laser & wire: microstructure and mechanical properties, in: *Proceedings of the NATO AVT-163 Specialists Meeting on Additive Technology For Repair of Military Hardware*, Bonn, Germany, 2009.
- [21] G.P. Dinda, L. Song, J. Mazumder, Fabrication of Ti-6Al-4V scaffolds by direct metal deposition, *Metall. Mater. Trans.* 39A (2008) 2914–2922.
- [22] C. Qiu, G.A. Ravi, C. Dance, A. Ranson, S. Dilworth, M.M. Attallah, Fabrication of large Ti-6Al-4V structures by direct laser deposition, *J. Alloy. Compd.* 629 (2015)

- 351–361.
- [23] J. Yu, M. Rombouts, G. Maes, F. Motmans, Material properties of Ti6Al4V parts produced by laser metal deposition, *Phys. Procedia* 39 (2012) 416–424.
- [24] N. Shamsaei, A. Yadollahi, L. Bian, S.M. Thompson, An overview of direct laser deposition for additive manufacturing; part II: mechanical behavior, process parameter optimization and control, *Addit. Manuf.* 8 (2015) 12–35.
- [25] Y. Zhai, H. Galarraga, D.A. Lados, Microstructure, static properties, and fatigue crack growth mechanisms in Ti-6Al-4V fabricated by additive manufacturing: LENS and EBM, *Eng. Fail. Anal.* 69 (2016) 3–14.
- [26] T. Hua, C. Jing, Z. Fengying, L. Xin, H. Weidong, Microstructure and mechanical properties of laser solid formed Ti-6Al-4V from blended elemental powders, *Rare Met. Mater. Eng.* 38/4 (2009) 0574–0578.
- [27] C. Liu, Y. Lu, X. Tian, D. Liu, Influence of continuous grain boundary  $\alpha$  on ductility of laser melting deposited titanium alloys, *Mater. Sci. Eng. A* 661 (2016) 145–151.
- [28] J. Alcisto, A. Enriquez, H. Garcia, S. Hinkson, T. Steelman, E. Silverman, P. Valdivino, H. Gigerenzer, J. Foyos, J. Ogren, J. Dorey, K. Karg, T. McDonald, O.S. Es-Said, Tensile properties and microstructures of laser-formed Ti-6Al-4V, *J. Mater. Eng. Perform.* 20/2 (2011) 203–212.
- [29] P.A. Kobryn, S.L. Semiatin, *Mechanical Properties of Laser-Deposited Ti-6Al-4V, AFRL/MLLMP*, pp. 179–186.
- [30] S. Zhang, X. Lin, J. Chen, W. Huang, Heat-treated microstructure and mechanical properties of laser solid forming Ti-6Al-4V alloy, *Rare Met.* 20/6 (2009) 537–544.
- [31] B. Baufeld, O. Van der Biest, R. Gault, Additive manufacturing of Ti-6Al-4V components by shaped metal deposition: microstructure and mechanical properties, *Mater. Des.* 31 (2010) 5106–5111.
- [32] B. Baufeld, Effect of deposition parameters on mechanical properties of shaped metal deposition parts, *J. Eng. Manuf.* 226 (2011) 126–136.
- [33] F. Wang, S. Williams, P. Colegrove, A.A. Antonysamy, Microstructure and mechanical properties of wire and arc additive manufactured Ti-6Al-4V, *Metall. Mater. Trans.* 44A (2012) 968–977.
- [34] M.J. Bermingham, D. Kent, H. Zhan, D.H. StJohn, M.S. Dargusch, Controlling the microstructure and properties of wire arc additive manufactured Ti-6Al-4V with trace boron additions, *Acta Mater.* 91 (2015) 289–303.
- [35] X. Shi, S. Ma, C. Liu, Q. Wu, J. Lu, Y. Liu, W. Shi, Selective laser melting-wire arc additive manufacturing hybrid fabrication of Ti-6Al-4V alloy: microstructure and mechanical properties, *Mater. Sci. Eng.* 684A (2017) 196–204.
- [36] T. Wang, Y.Y. Zhu, S.Q. Zhang, H.B. Tang, H.M. Wang, Grain morphology evolution behavior of titanium alloy components during laser melting deposition additive manufacturing, *J. Alloy. Compd.* 632 (2015) 505–513.
- [37] E. Brandl, V. Michailov, B. Viehweger, C. Leyens, Deposition of Ti-6Al-4V using laser and wire, part II: hardness and dimensions of single beds, *Surf. Coat. Technol.* 206 (2011) 1130–1141.
- [38] S.M. Thompson, L. Bian, N. Shamsaei, A. Yadollahi, An overview of direct laser deposition for additive manufacturing; part I: transport phenomena, modeling and diagnostics, *Addit. Manuf.* 8 (2015) 36–62.
- [39] X. Tan, Y. Kok, Y.J. Tan, M. Descoins, D. Mangelinck, S.B. Tor, K.F. Leong, C.K. Chua, Graded microstructure and mechanical properties of additive manufactured Ti-6Al-4V via electron beam melting, *Acta Mater.* 97 (2015) 1–16.
- [40] W. Xu, M. Brandt, S. Sun, J. Elambasseril, Q. Liu, K. Latham, K. Xia, M. Qian, Additive manufacturing of strong and ductile Ti-6Al-4V by selective laser melting via in situ martensite decomposition, *Acta Mater.* 85 (2015) 74–84.
- [41] S. Kou, *Welding Metallurgy*, Second edition, Wiley-Interscience, New Jersey, 2003.
- [42] S.A. David, J.M. Vitek, Correlation between solidification parameters and weld microstructures, *Int. Mater. Rev.* 34/5 (1989) 213–245.
- [43] I. Katzarov, S. Malinov, W. Sha, Finite element modeling of the morphology of  $\beta$  to  $\alpha$  phase transformation in Ti-6Al-4V alloy, *Metall. Mater. Trans.* 33A/4 (2002) 1027–1040.
- [44] S.M. Kelly, S.L. Kampe, Microstructural evolution in laser-deposited multilayer Ti-6Al-4V builds: part II. Thermal modeling, *Metall. Mater. Trans.* 35A/6 (2004) 1869–1879.
- [45] D. Hull, D.J. Bacon, *Introduction to Dislocations*, 5th edition, Butterworth-Heinemann, Oxford, 2011.
- [46] J. Weertman, J.R. Weertman, *Elementary Dislocation Theory*, Oxford University Press, New York, 1992.
- [47] P.A. Kobryn, E.H. Moore, S.L. Semiatin, The effect of laser power and traverse speed on microstructure, porosity, and build height in laser-deposited Ti-6Al-4V, *Scr. Mater.* 43 (2000) 299–305.
- [48] S.H. Wang, M.D. Wei, L.W. Tsay, Tensile properties of LBW welds in Ti-6Al-4V alloy at evaluated temperatures below 450 °C, *Mater. Lett.* 57 (2003) 1815–1823.
- [49] I. Karaman, G.G. Yapici, Y.I. Chumlyakov, I.V. Kireeva, Deformation twinning in difficult-to-work alloys during severe plastic deformation, *Mater. Sci. Eng. A* 410–411 (2005) 243–247.
- [50] Y.-H. Lin, S.-M. Wu, F.-H. Kao, S.-H. Wang, J.-R. Yang, C.-C. Yang, C.-S. Chiou, Microtwin formation in the  $\alpha$  phase of duplex titanium alloys affected by strain rate, *Mater. Sci. Eng. A* 528 (2011) 2271–2276.
- [51] W. Tirry, M. Nixon, O. Cazacu, F. Coghe, L. Rabet, The importance of secondary and ternary twinning in compressed Ti, *Scr. Mater.* 64 (2011) 840–843.
- [52] G.G. Yapici, I. Karaman, Z.-P. Luo, Mechanical twinning and texture evolution in severely deformed Ti-6Al-4V at high temperatures, *Acta Mater.* 54 (2006) 3755–3771.
- [53] M.H. Yoo, Slip, twinning, and fracture in hexagonal close-packed metals, *Metall. Trans.* A 12 (1981) 409–418.
- [54] Y.G. Liu, M.Q. Li, Stress-induced twinning of nanocrystalline hexagonal close-packed titanium in Ti-6Al-4V, *Mater. Lett.* 180 (2016) 47–50.
- [55] M. Preuss, J.Q. da Fonseca, V. Allen, D.G.L. Prakash, M.R. Daymond, Twinning in structural material with a hexagonal close-packed crystal structure, *J. Strain Anal. Eng. Des.* 45 (2010) 377–390.
- [56] N.E. Paton, W.A. Backofen, Plastic deformation of titanium at elevated temperatures, *Metall. Trans.* 1 (1970) 2839–2847.
- [57] M.H. Yoo, J.R. Morris, K.M. Ho, S.R. Agnew, Nonbasal deformation modes of HCP metals and alloys: role of dislocation source and mobility, *Metall. Mater. Trans.* 33A (2002) 813–822.
- [58] J.C. Williams, R.G. Baggerly, N.E. Paton, Deformation behavior of HCP Ti-Al alloy single crystals, *Metall. Mater. Trans.* 33A (2002) 837–850.
- [59] A.A. Antonysamy, J. Meyer, P.B. Prangnell, Effect of build geometry on the  $\beta$ -grain structure and texture in additive manufacture of Ti6Al4V by selective electron beam melting, *Mater. Charact.* 84 (2013) 153–168.
- [60] M. Simonelli, Y.Y. Tse, C. Tuck, Effect of the build orientation on the mechanical properties and fracture modes of SLM Ti-6Al-4V, *Mater. Sci. Eng. A* 616 (2014) 1–11.
- [61] M. Simonelli, Y.Y. Tse, C. Tuck, On the texture formation of selective laser melted Ti-6Al-4V, *Metall. Mater. Trans.* 45A (2014) 2863–2872.
- [62] J.C. Williams, M.J. Blackburn, A comparison of phase transformations in 3 commercial titanium alloys, *ASM Trans. Q.* 60 (1967) 373–383.
- [63] F.J. Gil, J.M. Manero, J.A. Planell, Decomposition of  $\alpha'$  martensite plates of Ti-6Al-4V alloy at different annealing temperatures and heat treatment times, in: P.A. Blankensop, W.J. Evans, H.M. Flower (Eds.), *Titanium 1995, Science and Technology*, The Institute of Materials, London, UK, 1996, pp. 2454–2461.
- [64] U. Pinsook, G.J. Ackland, Atomistic simulation of shear in a martensitic twinned microstructure, *Phys. Rev. B* 62 (2000) 5427–5434.
- [65] J.R. Morris, K.M. Ho, Molecular dynamic simulation of a homogeneous bcc  $\rightarrow$  hcp transition, *Phys. Rev. B* 63 (2001) 224116.
- [66] S. Banerjee, P. Mukhopadhyay, Phase transformations: examples from titanium and zirconium alloys, *Pergam. Mater. Ser.* 12 (2007).
- [67] D. Banerjee, J.C. Williams, Perspectives on titanium science and technology, *Acta Mater.* 61 (2013) 844–879.
- [68] B. Appolaire, L. Hélicher, E. Aebly-Gautier, Modelling of phase transformation kinetics in Ti alloys – isothermal treatments, *Acta Mater.* 53 (2005) 3001–3011.
- [69] Z. Sun, S. Guo, H. Yang, Nucleation and growth mechanism of a  $\alpha$ -lamellae of Ti alloy TA15 cooling from an  $\alpha + \beta$  phase field, *Acta Mater.* 61 (2013) 2057–2064.
- [70] C.M. Liu, H.M. Wang, X.J. Tian, H.B. Tang, D. Liu, Microstructure and tensile properties of laser melting deposited Ti-5Al-5Mo-5V-1Cr-1Fe near  $\beta$  titanium alloy, *Mater. Sci. Eng.* 586A (2013) 323–329.
- [71] D. Bhattacharyya, G.B. Viswanathan, H.L. Fraser, Crystallographic and morphological relationships between  $\beta$  phase and the Widmanstätten and allotriomorphic  $\alpha$  phase at special  $\beta$  grain boundaries in an  $\alpha/\beta$  titanium alloy, *Acta Mater.* 55 (2007) 6765–6778.
- [72] N. Brodusch, R. Gauvin, The qualitative f-ratio method applied to electron channeling-induced x-ray imaging with an annular silicon drift detector in a scanning electron microscope in the transmission mode, *J. Microsc.* 00/0 (2017) 1–11.
- [73] V. Raghavan, Al-Ti-V (aluminum-titanium-vanadium), *J. Phase Eval.* 26 (2005) 276–279.
- [74] A.V. Sergueeva, J. Zhou, B.E. Meacham, D.J. Branagan, Gage length and sample size effect on measured properties during tensile testing, *Mater. Sci. Eng. A* 526 (2009) 79–83.
- [75] P. Åkerfeldt, M.-L. Antti, R. Pederson, Influence of microstructure on mechanical properties of laser metal wire-deposited Ti-6Al-4V, *Mater. Sci. Eng. A* 674 (2016) 428–437.